PNAS RESEARCH ARTICLE | SUSTAINABILITY SCIENCE

Moisture-driven carbonation kinetics for ultrafast CO_2 mineralization

Yining Gao[a,b,1], Yong Tao[a,b,1,2], Gen Li[a,b], Peiliang Shen[a,b,2], Roland J.-M. Pellenq[c], and Chi Sun Poon[a,b,2]

Affiliations are included on p. 8.

Edited by Alexandra Navrotsky, Arizona State University, Tempe, AZ; received September 6, 2024; accepted November 18, 2024

CO_2 mineralization, a process where CO_2 reacts with minerals to form stable carbonates, presents a sustainable approach for CO_2 sequestration and mitigation of global warming. While the crucial role of water in regulating CO_2 mineralization efficiency is widely acknowledged, a comprehensive understanding of the underlying mechanisms remains elusive. This study employs a combined experimental and atomistic simulation approach to elucidate the intricate mechanisms governing moisture-driven carbonation kinetics of calcium-bearing minerals. A self-designed carbonation reactor equipped with an ultrasonic atomizer is used to meticulously control the water content during carbonation experiments. Grand Canonical Monte Carlo simulations reveal that maximum CO_2 uptake occurs at a critical water content where the initiation of capillary condensation significantly enhanced liquid–gas interactions. This phenomenon leads to CO_2 adsorption–driven ultrafast carbonation at an optimal moisture content (0.1 to 0.2 g/g, water mass ratio to total wet mass of the mineral). A higher moisture content decimates the carbonation rate by crippling CO_2 intake within mineral pores. However, at exceptionally high moisture levels, the carbonation reaction sites shift from internal mesopores to the grain surface. This results in surface dissolution–driven ultrafast carbonation, attributed to the monotonically decreasing free energy of dissolution with increasing surface water thickness, as revealed by metadynamics simulations. This study provides a fundamental and unified understanding of the multifaceted role of water in mineral carbonation, paving the way for optimizing ultrafast CO_2 mineralization strategies for global decarbonization efforts.

CO_2 mineralization | moisture impact | carbonation kinetics | atomistic simulations

CO_2 mineralization offers a long-term and secure decarbonization strategy to help mitigate global warming (1–3). In situ CO_2 mineralization involves the injection of highly concentrated CO_2 underground for physical and chemical trapping, which takes decades to thousands of years for the geological conversion of CO_2 (1, 4, 5). On the other hand, ex situ mineralization utilizes enhanced mineral carbonation reactions with reactive ores (6) or solid wastes (7–10). The resulting carbonation products are either disposed of or recycled (Fig. 1*A*) (11). Both approaches face a significant challenge in achieving desirable CO_2 mineralization efficiency at acceptable economic costs (12). Recent findings have revealed a substantial gap between the operational and announced CO_2 capture and storage capacities, underscoring the challenges faced in economically feasible real-world applications (Fig. 1*B*). Indeed, current CO_2 mineralization technologies consume a lot of water and energy (13, 14). In particular, experimental studies and applications employ different water contents and states, such as vapor (15–17), mist (18), or bulk liquid (19–21) as depicted in Fig. 1*C*. Previous studies have highlighted the crucial role of water as a medium for various reactions (dissolution, solvation, diffusion, precipitation, nucleation, etc.) during the carbonation process, which governs the overall mineral carbonation kinetics (22, 23). On the other hand, the influence of relative humidity on mineral carbonation efficiency presents a complex picture with varying findings. While most studies suggest optimal carbonation efficiency at low relative humidity (40 to 60%) (24, 25), some research points to maximum efficiency at high relative humidity (>90%) (16, 26). Notably, high carbonation efficiency is also observed in aqueous carbonation scenarios where the mineral reacts with CO_2 in the bulk water (27–30). This discrepancy highlights the different carbonation pathways altered by water content (22). However, the fundamental mechanisms through which water supply acts as a facilitator in the mineral carbonation process are not yet fully understood. A unified understanding of the role of water in different carbonation conditions has not been provided.

For mineral carbonation in an aqueous solution, liquid water penetrates mesopores within the minerals through capillary imbibition and flow (31–33), which transports

Significance

Understanding how water impacts mineral carbonation kinetics holds great significance in pursuing high-efficiency CO_2 mineralization in global decarbonization practices. We utilize a meticulously designed carbonation reactor coupled with atomistic simulations to unravel the moisture-driven mineral carbonation mechanisms. It is observed that maximum CO_2 uptake occurs at a critical water content where the onset of capillary condensation intensifies liquid–gas interactions, leading to adsorption-driven ultrafast carbonation at an optimal moisture content of 0.1 to 0.2 g/g (water to wet mineral mass ratio). Conversely, exceptionally high moisture shifts carbonation kinetics to a surface dissolution–driven process. These findings provide a unified explanation for the often-debated optimal carbonation conditions in experiments and offer crucial guidance for harnessing moisture control to achieve efficient CO_2 mineralization.

Author contributions: Y.G., Y.T., and P.S. designed research; Y.G. and Y.T. performed research; Y.G., Y.T., and G.L. contributed new reagents/analytic tools; Y.G., Y.T., R.J.-M.P., and C.S.P. analyzed data; Y.G., Y.T., G.L., P.S., R.J.-M.P., and C.S.P. reviewed the paper; and Y.G. and Y.T. wrote the paper.

The authors declare no competing interest.

This article is a PNAS Direct Submission.

[1]Y.G. and Y.T. contributed equally to this work.

[2]To whom correspondence may be addressed. Email: yong.tao@polyu.edu.hk, peiliang.shen@polyu.edu.hk, or chi-sun.poon@polyu.edu.hk.

This article contains supporting information online at https://www.pnas.org/lookup/suppl/doi:10.1073/pnas.2418239121/-/DCSupplemental.

Published December 30, 2024.

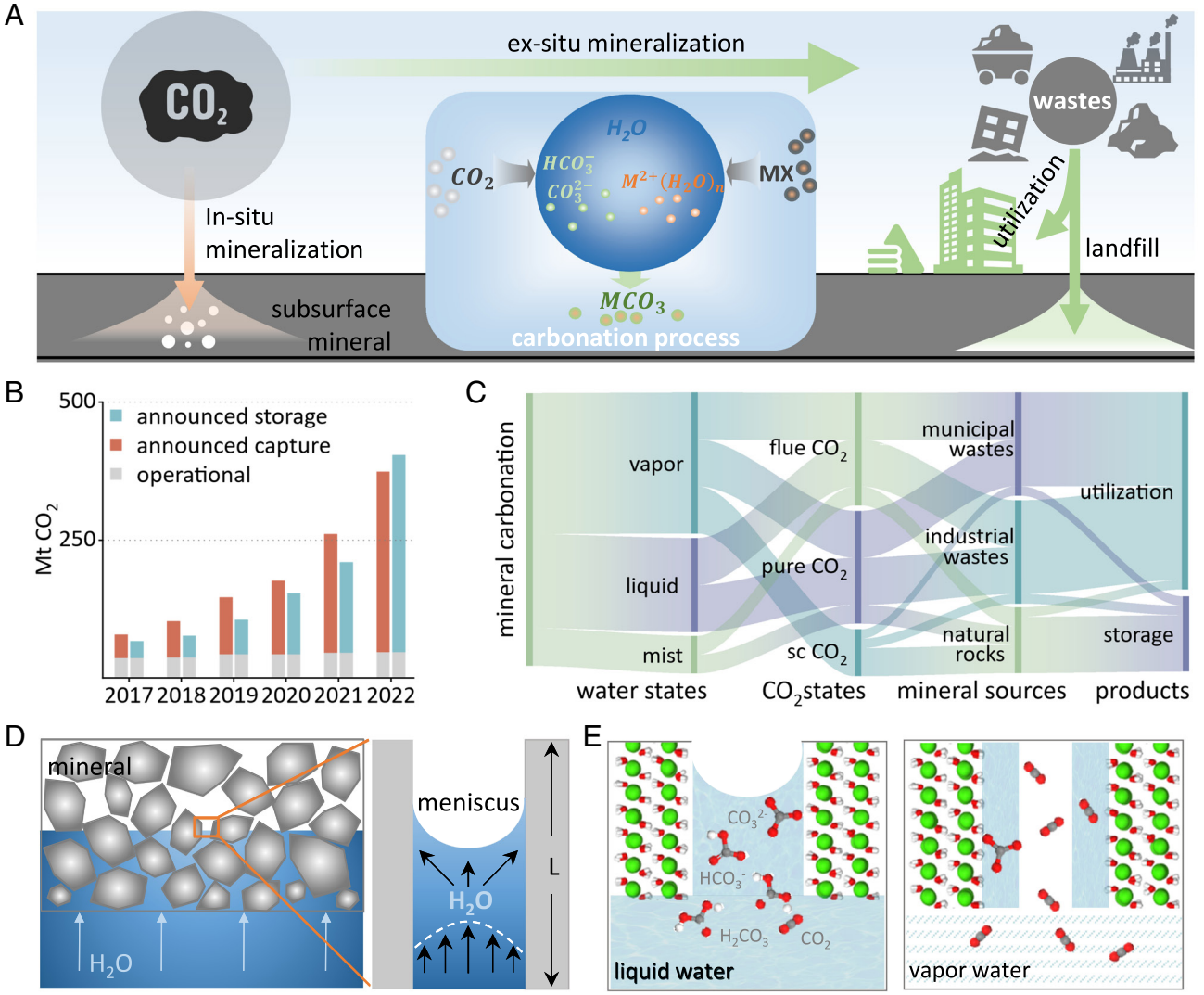

Fig. 1. Schematic multiscale perspectives of CO_2 mineralization. (*A*) The in situ and ex situ CO_2 mineralization schemes with their shared basic water-mediated carbonation processes, i.e., mineral dissolution, CO_2 speciation, and carbonate precipitation. MX represents alkaline earth metal compounds. (*B*) Comparison of globally announced and operational capacity on CO_2 storage and capture in recent years (Source: International Energy Agency). (*C*) Schematic classification of CO_2 mineralization based on water and CO_2 sources and product utilization. (*D*) Schematic diagram illustrating capillary permeation during mineral carbonation. (*E*) Moisture-mediated CO_2 transport within capillary pores in minerals. CO_2 migrates in saturated pores in the form of hydrated ions as the meniscus advances, while gas CO_2 can diffuse in unsaturated pores.

carbonate/bicarbonate species into the internal pores for chemical reactions (Fig. 1*D*). The capillary imbibition kinetics can be described by the classical Lucas–Washburn equation under the assumption of laminar flow and no gravity (34, 35):

$$L = kt^{1/2} = \sqrt{\frac{\gamma r \cos\theta}{2\eta}}\, t^{1/2}, \qquad [1]$$

where L and t represent the penetration distance and time, respectively. k denotes the capillarity front coefficient which relates to the geometry and roughness of the capillary wall and the properties of the liquid. r, η, γ, and θ are the pore radius, dynamic viscosity of the liquid, surface tension of the liquid, and the contact angle at the three-phase contact point, respectively. This equation provides an estimate of the advancing rate of the meniscus, which, to some extent, reflects the rate of CO_2 penetration into the materials. However, for mineral carbonation with a limited water supply, most internal mesopores are not fully saturated with water, where the external CO_2 penetrates the materials in a different manner (Fig. 1*E*). In our previous experimental studies, it has been observed that not only the transport behaviors but also the nucleation and growth of carbonation products are regulated with water content during carbonation (18, 23) Therefore, understanding the relationship between carbonation kinetics and mineral moisture is crucial for formulating high-efficiency and cost-effective carbonation solutions for real-world applications at scale.

In this study, we aim to reveal the intricate role of moisture dynamics in enhancing mineral carbonation reactions to reveal the optimal conditions for ultrafast CO_2 mineralization. Taking recycled concrete powder (RCP), one of the most commonly used alkaline solid wastes for CO_2 mineralization (11, 36–38), as a representative example, we conducted comprehensive carbonation experiments under various water contents using our developed carbonation apparatus (18) that allows precise control of the water flux during carbonation. Advanced molecular simulation methods including Grand Canonical Monte Carlo (GCMC) and well-tempered metadynamics were employed to unveil the fundamental mechanisms of water-mediated carbonation reactions. This study provides comprehensive insights into moisture-driven thermodynamics and kinetics of mineral carbonation, suggesting optimal

water conditions for achieving ultrafast CO_2 mineralization in global decarbonization practices.

Results and Discussion

Effect of Water Flux on Carbonation Efficiency and Pore Structure. We further upgraded our recently developed carbonation system (Fig. 2*A*) (18) with precise control over water flux to investigate the moisture-driven carbonation kinetics of RCP. The reaction chamber is integrated with an ultrasonic atomizer nozzle to generate micron-sized mist droplets, driven by a high-precision peristaltic pump that delivers adjustable water flux to achieve the desired moisture conditions. Within the reaction chamber, the custom-designed specimen holder ensures uniform exposure of the samples to the water mist/CO_2 mixed atmosphere. Inlet and outlet ports enable precise control of CO_2 gas introduction and removal, facilitating carbonation reactions under well-defined and reproducible conditions. All carbonation experiments are conducted at ambient temperature and pressure. To accurately characterize water involvement in our experimental setup, we adopt two complementary metrics: the externally controlled parameter termed water flux (J, g/min) and the resultant moisture content (w, g/g) of the mineral sample after water infiltration. w is defined as the proportion of water mass to the total mass in the sample, i.e., $w = m_{water}/(m_{solid} + m_{water})$ (16, 30, 39). Fig. 2*B* delineates the correlation between the input water flux and the resulting mineral moisture content at a constant time interval of 15 min.

Quantifying carbonation product formation under controlled water flux conditions is essential for understanding the mechanistic carbonation pathways. We characterized the carbonation products formed under different water fluxes (0 to 2 g/min for 15 min) using X-ray Diffraction (XRD) analysis (*SI Appendix*, Fig. S1). The corresponding quantitative phase composition via Rietveld refinement analysis is depicted in Fig. 2*C* and *SI Appendix*, Table S1. The original RCP consists primarily of amorphous calcium silicate hydrates (A-hydrates) and portlandite (calcium hydroxide, denoted as CH), with smaller amounts of clinker phases, calcite, monocarbonates, and other crystalline hydration phases (C-hydrates) such as hydrogarnet and hydrotalcite. To facilitate the analysis of the carbonation process, we focused on two key substances: CH (the most CO_2-reactive phase in RCP) and calcite (the main carbonation product). Fig. 2 *D* and *E* shows the selected XRD patterns of CH and calcite under different water fluxes, respectively. The intensities of these peaks have been normalized to the peak intensity of the ZnO marker phase, with the maximum intensity set to unity. The color scaling represents this normalized intensity, ranging from 0 to 1. From the XRD data (Fig. 2 *D* and *E* and *SI Appendix*, Table S1), it is evident that when J is less than 0.05 g/min, the content of CH decreases with an increase in J. However, when J reaches 0.4 g/min, the CH content initially increases and then continuously decreases as J increases. Correspondingly, at the initial stages, as J increases from 0 to 0.1 g/min, the content of calcite rises. This suggests that a slight increase in water flux enhances the carbonation reactions. As J increases from 0.1 to 0.4 g/min, the calcite content decreases, which indicates a higher water content impedes the carbonation process. However, the calcite content starts to increase again when J exceeds 0.4 g/min. The observed trends imply the complex influence of water content on mineral carbonation kinetics, which will be further elucidated in the following sections.

To illustrate the changes in pore structures of RCP after carbonation, we determined the pore size distribution and specific surface area using the Brunauer–Emmett–Teller (BET) method with N_2 gas adsorption/desorption. Fig. 2*F* demonstrates that the content of small mesopores (<20 nm) increases after carbonation, particularly under a large water flux (e.g., 2 g/min), which is probably due to the densification of large mesopores by the carbonation products. The barely changed pore size distribution for the carbonated samples with J = 0.05 and 0.4 g/min is due to the limited carbonate formation (Fig. 2*C*). Moreover, the adsorption/desorption isotherm hysteresis suggests the mesopores within RCP belong to the V-type slit pore of the IUPAC classification (*SI Appendix*, Fig. S2). The width of isotherm hysteresis becomes larger for the highly carbonated samples under an appropriate water flux, indicating an increase in the size of nanopores (*SI Appendix*, Fig. S2). The specific surface area and cumulative pore volume (Fig. 2*G*) increase from the initial 7.64 $m^2\ g^{-1}$ and 0.05 $m^3\ g^{-1}$ to 11.45 $m^2\ g^{-1}$ and 0.06 $m^3\ g^{-1}$, respectively, for J = 0.1 g/min, while the average pore size decreases from 21.95 nm to 17.14 nm. With a larger water flux (J = 2 g/min), the changes are even more significant, featuring increased surface area and pore volume of 22.05 $m^2\ g^{-1}$ and 0.07 $m^3\ g^{-1}$, and reduced average pore size to 12.31 nm. This is in line with Fig. 2*F*, which states that the content of smaller mesopores increased after carbonation. The accumulative pore volume analysis reveals two important findings (Fig. 2*H*). First, carbonation increases the volume of small mesopores (<50 nm), which can be utilized as a qualitative indicator of the carbonation degree because Fig. 2 *C* and *H* forecasts precisely the same effect of water flux on the carbonation efficiency of RCP. Second, while the formed calcite contents are similar (Fig. 2*C*), the pore volume for J = 2 g/min is notably larger than that for J = 0.1 g/min. This may be attributed to the accumulation of carbonates on the grain surface rather than within the mesopores in the near-aqueous carbonation scenario, as observed in the carbonation experiments (18).

Moisture-Driven Carbonation Kinetics. Since the carbonation rate of RCP is highly dependent on the water supply (Fig. 2*C*), we conducted orthogonal experiments of RCP carbonation using different water fluxes (J, g/min) and reaction times (t, min). The tabulated results are presented in *SI Appendix*, Table S2. Fig. 3*A* shows the carbonation degree (η, %) as a function of t and J, i.e., $\eta(t, J)$. η was defined as the mass ratio of carbonated calcium oxide to the total equivalent calcium oxide in RCP (*SI Appendix*, Table S3). To analyze the impact of moisture on the carbonation kinetics, we calculated the change rate in η with respect to t ($r_t(t, J)$) and J ($r_J(t, J)$) by performing partial differentiation (Fig. 3 *B* and *C*). $r_t(t, J)$ represents the increase in the carbonation degree per unit time (min) under a specific water flux and reaction time. Similarly, $r_J(t, J)$ represents the increase in the carbonation degree per unit water flux (g/min) under a specific water flux and reaction time.

Generally, η increases with t while J shows a twofold effect on η (Fig. 3*A*). Two extreme values of η appear around J = 0.1 g/min and J > 1 g/min, respectively. η increases with J within the range of $0 < J \leq 0.1$ g/min, beyond which, as J increases, η initially decreases and then increases. This illustrates that the amount of water strongly influences the carbonation process of minerals (16, 40). First, we discuss the relationship between the carbonation rate $r_t(t, J)$ and reaction time under different water fluxes (Fig. 3*B*). $r_t(t, J)$ is significant within the first 15 min of reaction and experiences an abrupt drop thereafter. This is understandable because the accumulated carbonation products on the mineral surface hinder the further dissolution and carbonation of the mineral. When the water flux is less than 0.02 g/min, $r_t(t, J)$ is not sensitive to the reaction time, which suggests that the carbonation of RCP requires a minimal water amount for activation. This agrees with previous

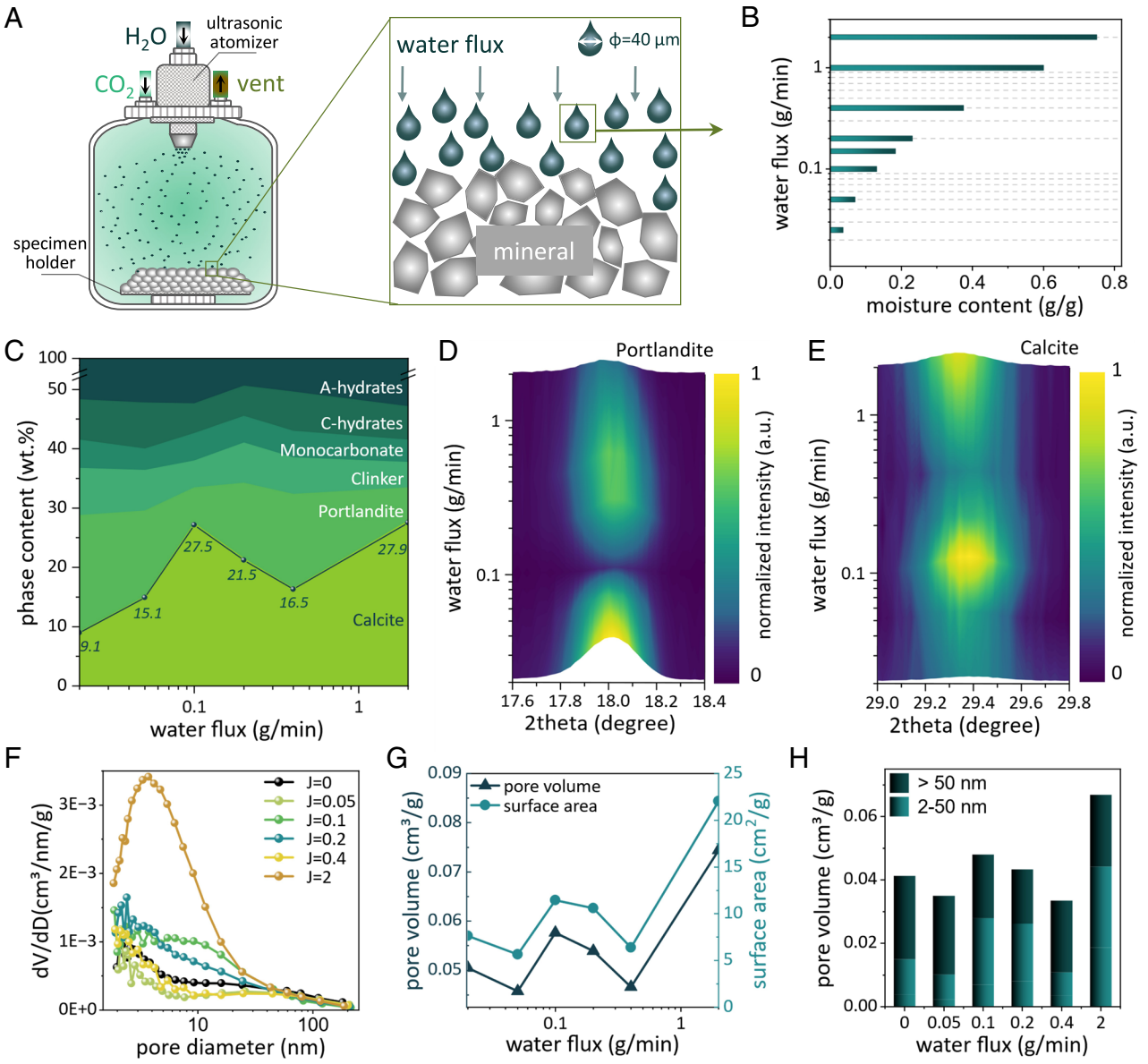

Fig. 2. Influence of water flux on phase composition and pore structures of carbonated RCP. (*A*) Schematic of the carbonation setup, featuring a constant CO_2 flow and controlled water flux delivered as micron-sized droplets. (*B*) Relationship between water flux and the accumulated moisture content within the RCP sample after a 15-min carbonation period. Moisture content is defined as the ratio of water mass to the total mass of the wet material. (*C*) Phase composition of carbonated RCP after 15 min. The sample with zero water flux represents the original, uncarbonated RCP. The black line highlights the variation in calcite content. (*D* and *E*) Main X-ray diffraction patterns of portlandite and calcite in carbonated RCP at different water fluxes. Peak intensities are normalized to the ZnO marker phase, with the maximum intensity set to unity and represented by the color scale. (*F* and *G*) Pore size distribution, cumulative pore volume, and specific surface area of carbonated RCP at various water fluxes (*J*, g/min). (*H*) Changes in the volume of small pores (2 to 50 nm) and large pores (>50 nm) in carbonated RCP at various water fluxes. All data presented are for samples after a 15-min carbonation period. All presented data correspond to carbonated RCP after 15 min carbonation under different water fluxes.

experimental studies of Galan et al. (40), where they found that the carbonation of cement paste was barely observed at a low relative humidity of 11%. At a constant water flux of 0.1 g/min, $r_t(t,J)$ reaches the maximum at about 10 min. When the water flux is greater than 1 g/min, the maximum $r_t(t,J)$ shifts to about 5 min from the beginning, which indicates that fast carbonation happens at the very beginning. This is consistent with the observation in the aqueous carbonation experiments (where the solids are immersed in the aqueous solution) that the carbonation rate decreases with time from the very beginning (30). Overall, the maximum $r_t(t,J)$ advances with increased water flux.

Now, we discuss the relationship between the carbonation rate $r_J(t,J)$ and the water flux at different reaction times (Fig. 3*C*). First, $r_J(t,J)$ varies dramatically with the water flux when $J < 0.2$ g/min. Beyond this threshold, $r_J(t,J)$ is not sensitive to the change in water flux, because the carbonation environment gradually approaches the aqueous carbonation conditions where water supply is no longer a reaction limiting factor. Within the first 10 min, the water flux has a negligible effect on $r_J(t,J)$ due to the minimal cumulative water volume and the relatively low carbonation degree of RCP. (Fig. 3*A*). For a 15-min carbonation reaction, the maximum $r_J(t,J)$ occurs at a water flux of ~0.07 g/min, beyond which $r_J(t,J)$ declines sharply and even becomes negative when the water flux exceeds 0.1 g/min. This indicates that a water flux over 0.1 g/min results in a reduction in the carbonation degree as shown in Fig. 3*A*. When the water flux exceeds 0.17 g/min, $r_J(t,J)$ exhibits a gradual increase in response to the water flux, albeit with a

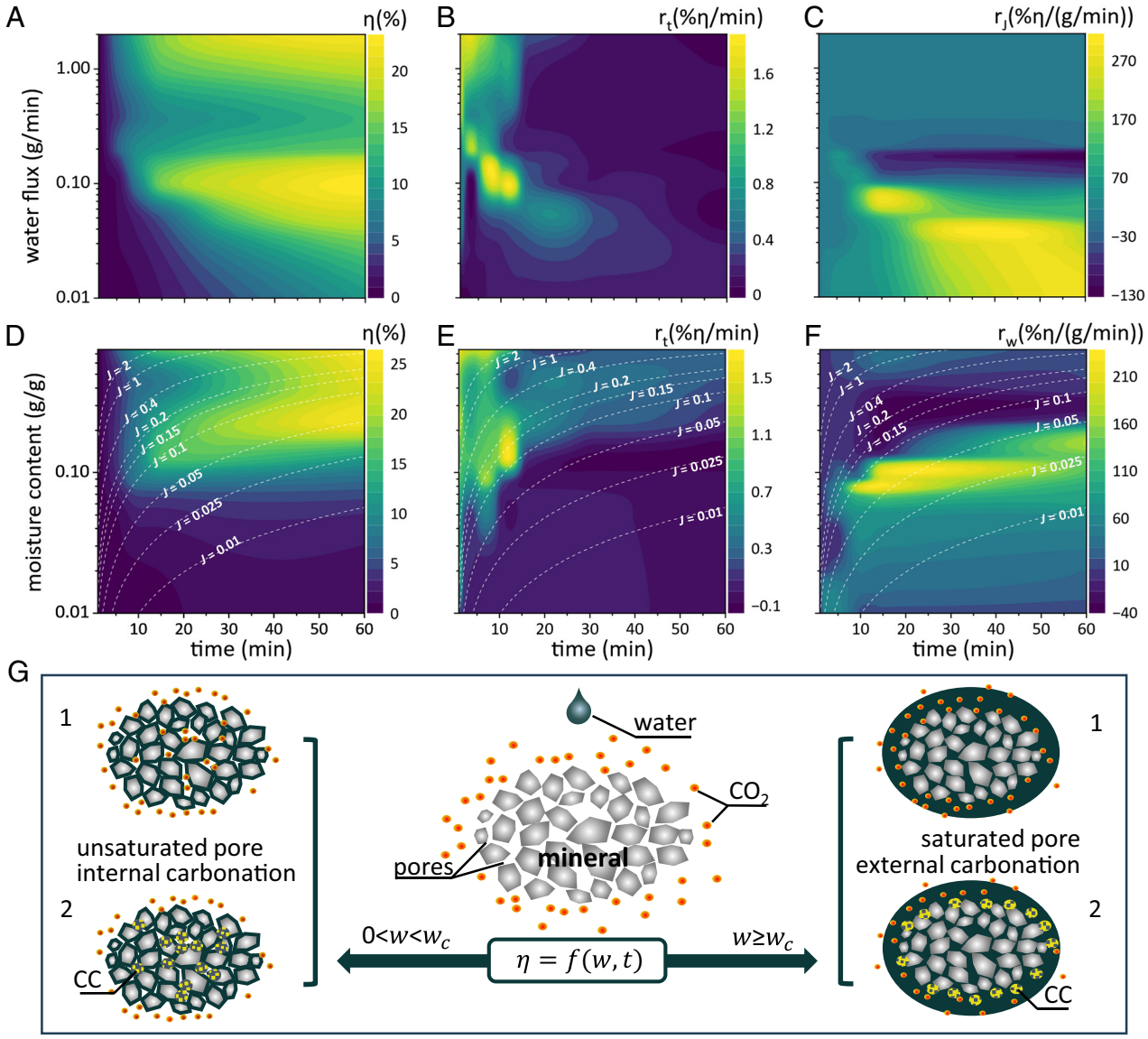

Fig. 3. Carbonation kinetics of RCP at different water supplies. (*A*) Carbonation degree (η) as a function of water flux (J) and carbonation time (t). (*B*) The calculated carbonation rate with respect to t ($r_t(t,J)$), representing the increase in η per unit t under a specific J and t. (*C*) The calculated carbonation rate with respect to J ($r_J(t,J)$), denoting the increase in η per unit J under a specific J and t. (*D*) Carbonation degree as a function of moisture content (w) and t. (*E*) The calculated carbonation rate with respect to t, i.e., $r_t(t,w)$. (*F*) The calculated carbonation rate with respect to w, i.e., $r_w(t,w)$. (*G*) Schematic illustration of different carbonation scenarios divided by a critical moisture content (w_c): internal carbonation within the unsaturated mesopores and external carbonation on the mineral surface.

relatively gentle variation. For longer carbonation durations (e.g., 30 min), the relationship between $r_J(t,J)$ and water flux displays a similar behavior as described above. However, the maximum value is attained at a lower water flux (~0.04 g/min). Overall, as the carbonation reaction time increases, the water flux required to maximize $r_J(t,J)$ gradually decreases. Consequently, the carbonation rate can be optimized at various reaction times by precisely controlling the water flux.

To establish the relationship between carbonation kinetics and the materials' states, we calculated the moisture content (w) of the samples during carbonation. Since the accumulative water is determined by the water flux J and carbonation time t, we converted the J,t-dependent $\eta(t,J)$ into w,t-dependent $\eta(t,w)$ as shown in Fig. 3*D*. In analogy to Fig. 3 *B* and *C*, the change rate in η with respect to t ($r_t(t,w)$) and w ($r_w(t,w)$) were calculated by performing partial differentiation (Fig. 3 *E* and *F*). $r_t(t,w)$ represents the increase in the carbonation degree per unit time under a specific reaction time and final moisture content. Similarly, w ($r_w(t,w)$) represents the increase in the carbonation degree per unit of moisture content. Because w and t are related, the evolution of w with t at different water fluxes is illustrated in Fig. 3 *D*–*F* to facilitate the understanding of $\eta(t,w)$, $r_t(t,w)$, and $r_w(t,w)$.

Similar to $\eta(t,J)$, $\eta(t,w)$ increases with t while w shows a two-fold effect on η with two local maxima at $w = 0.2$ g/g and $w >> 0.5$ g/g (Fig. 3*D*), which highlights the importance of controlling the moisture content of the mineral for efficient carbonation. Fig. 3*E* spots the critical moisture content of 0.1 to 0.2 g/g for the most efficient carbonation of RCP. Based on a comprehensive analysis of the carbonated samples including the carbonation rate (Fig. 3*E*), the surface wetness, and the carbonation product distribution (*SI Appendix*, Fig. S3), 0.1 to 0.2 g/g is the optimal moisture content for mineral carbonation at low water content conditions where the solids' surface is dry, and the carbonation reactions primarily take place in the mesopores between the nanograins. In addition, $r_t(t,w)$ is large for extremely high moisture content (>0.7 g/g), which corresponds to the aqueous carbonation scenario where solid dissolution is significant. As for the

relationship between carbonation rate and moisture content under different reaction times (Fig. 3*F*), $r_w(t, w)$ varies greatly within the moisture content of 0.4 g/g and becomes less sensitive to higher moisture contents. This indicates that an extremely high water content may yield a high carbonation degree but results in inefficient utilization of water, which leads to substantial water consumption and energy input for wastewater treatment in practical applications.

Based on the above analysis, we summarize the effect of water on the carbonation process of minerals. Water is involved in the three main carbonation processes of calcium-bearing minerals (CaX, X represents oxygen, hydroxide, silicate, sulfate, and other anion groups.), i.e., calcium dissolution (Eq. **2**), CO_2 speciation (Eqs. **3**–**5**), and calcium carbonate precipitation (Eq. **6**).

$$CaX + mH_2O \rightarrow Ca^{2+} + 2OH^- + H_2X + (m-2)H_2O, \quad [2]$$

$$CO_2 + mH_2O \leftrightarrow H_2CO_3 + (m-1)H_2O, \quad [3]$$

$$H_2CO_3 + (m-1)H_2O \leftrightarrow H^+ + HCO_3^- + (m-1)H_2O, \quad [4]$$

$$HCO_3^- + (m-1)H_2O \leftrightarrow H^+ + CO_3^{2-} + (m-1)H_2O, \quad [5]$$

$$Ca^{2+} + CO_3^{2-} \rightarrow CaCO_3, \quad [6]$$

$$CaX + CO_2 + 2mH_2O \rightarrow CaCO_3 + H_2X + (2m-1)H_2O. \quad [7]$$

Although the overall carbonation reaction releases the water it consumed at the beginning (Eq. **7**), the amount of water regulates the carbonation environments that mediate the kinetics of subsequent reactions toward the overall carbonation efficiency. We can use a critical moisture content (w_c) to divide the carbonation conditions into two scenarios (Fig. 3*G*). When $w < w_c$, the water droplets permeate the internal mesopores of the mineral to form thin water film on the pore walls, which provides an ideal humid environment for CO_2 reacting with the dissolved calcium ions. In this condition, carbonation kinetics is sensitive to the moisture content as it alters the water film thickness in the mesopores which controls the dissolution kinetics of calcium ions and the transport of CO_2. Therefore, an optimal moisture content is expected for the highest carbonation rate (Fig. 3*E*). When $w >> w_c$, the sufficient water amount saturates most of the internal mesopores, blocking the permeation of CO_2. However, this water saturation state favors the mineral dissolution and diffusion of dissolved calcium ions to the outer surface of minerals, which diverts the primary carbonation reaction zone from internal mesopores to the outer surface. In this condition, the initially high carbonation rate decreases rapidly with carbonation time because the accumulation of carbonation products on the mineral surface impedes calcium ion leaching (*SI Appendix*, Fig. S3). Overall, the pursuit of optimal conditions under low moisture contents is more delicate yet attractive from the perspective of practical applications at scale. The fundamental mechanisms of the optimal unsaturated states of the mesopores for efficient carbonation are revealed in the next section.

Atomistic Mechanisms of Moisture-Driven Carbonation Thermodynamics. The packing of nanograins forms the multiscale pores within minerals. The water saturation state of these pores is determined by the equilibrium relative humidity, as the Kelvin equation describes (41). When the relative humidity is below 100%, water completely fills the smaller pores through capillary condensation yet only forms water films of various thicknesses in the larger pores (42). These nanometer-thick water films provide both solid/liquid and liquid/gas interfaces, serving as nano-reactors for mineral carbonation (43). The efficiency of mineral carbonation depends on the sufficient supply of reactants (i.e., metal ions and CO_2) within the nanoscale water films (22). The ideal state of carbonation would be a continuous dissolution of metal ions from the solid surface into the water film, with CO_2 being transported into the water film from the exterior. Both factors are influenced by the state of water within mesopores. To this end, we studied the impact of water content on CO_2 adsorption behavior and the thermodynamics of surface calcium ion dissolution in a 4 nm slit pore of CH through molecular dynamics simulation (Fig. 4). Actual minerals contain pores ranging from nanometers to micrometers (44), and their surface properties, however, are the same at the molecular scale. The water saturation states of these pores follow the Kelvin equation, except for particularly small pores (<2 nm), where the strong interactions between the upper and lower pore walls cause the physicochemical properties of water within the pores to deviate significantly from its normal state (45, 46).Therefore, we chose a 4 nm slit pore, which retains the basic properties of all mesopores while significantly reducing the computational load of molecular simulations (47). It should be noted that the water content in the simulation models, different from the moisture content described in Fig. 3, is defined as the molar ratio of water molecules of the water film to the maximum water molecules that fill the entire 4 nm pore.

The amount of CO_2 adsorption in the CH pore increases with the water content and reaches the maximum at 83.3% water content. Beyond this critical water content, the CO_2 intake decreases sharply (Fig. 4*A*). This implies an optimal water content in the CH pore that maximizes CO_2 adsorption. A higher water content is detrimental to CO_2 intake and, consequently, to the mineral carbonation process. Further analyses reveal that these observations are attributed to the hydrophobic nature of CO_2. CO_2 molecules preferentially accumulate at the liquid/gas interface within the CH pore (Fig. 4 *B* and *D*). Within a specific range of water content, the liquid/gas interface is always present, and the amount of dissolved CO_2 gradually increases with the water layer thickness, leading to a slow rise in the total CO_2 intake. When the water content reaches 83.3%, capillary condensation (i.e., the water film on the pore walls suddenly fills the entire pore) occurs in the CH pores, where the pore water is filled with density-fluctuation metastable water (*SI Appendix*, Fig. S4). This condition intensely enhances the liquid/gas interactions and results in a great CO_2 intake (Fig. 4*A*). A higher water content leads to the disappearance of the liquid/gas interface and a consequent sharp drop in CO_2 adsorption.

In contrast to CO_2 adsorption behavior, the increase in water content in the pore almost monotonically promotes the dissolution of calcium ions (Fig. 4*E*). The free energy barrier for calcium dissolution decreases from 306.7 kJ/mol to 71.8 kJ/mol as the water content increases from 16.7 to 100%. This is related to the mobility of surface-adsorbed water. Due to the strong adsorption of the thin water layer by the solid surface, the diffusion coefficient of water at 16.7% water content is extremely low (Fig. 4*C*), meaning that the surface water is somewhat "frozen." This condition is not conducive to calcium dissolution, as it requires the continuous exchange of water molecules in the first coordination shell of the calcium ion (48). As the water content increases, the thickness of the surface water film continues to grow. The water molecules at the liquid/gas interface become increasingly distant from the solid surface, thus weakening the adsorption effect of the surface and gradually increasing their mobility, leading to a rise in the average diffusion coefficient of water in the pore. The higher diffusion coefficients at 66.7% and 83.3% water contents compared to fully saturated pores (100% water content) are due to the liquid/gas

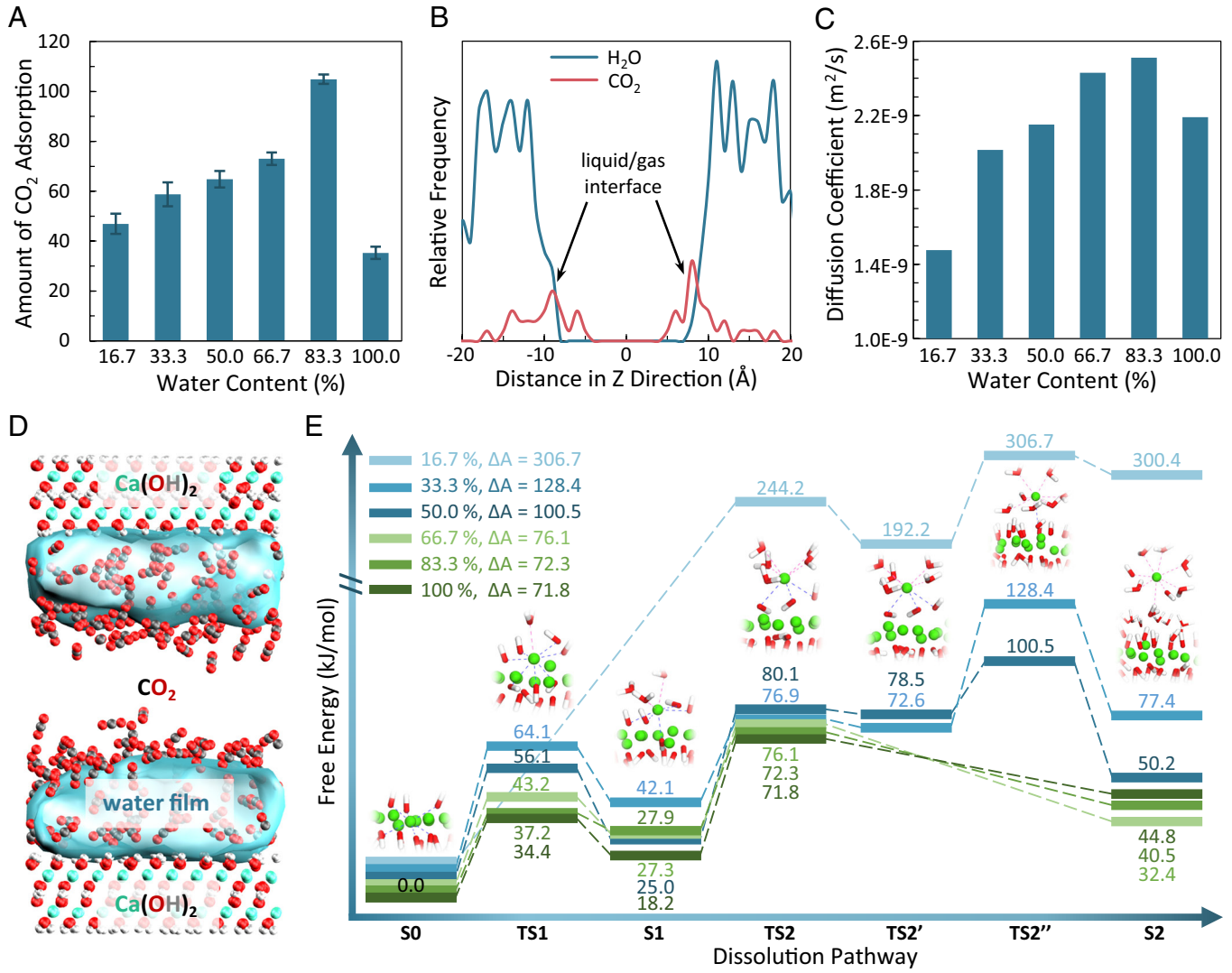

Fig. 4. Effect of water content on the carbonation process within a 4 nm CH slit pore. (*A*) Amount of CO_2 adsorption in the CH pore across different water content levels. Water content is quantified as the ratio of the water volume in the pore to the entire pore volume. (*B*) Water and CO_2 distributions within the pore at 50% water content, examined in the direction perpendicular to the pore. (*C*) Water self-diffusion coefficients within the pore under different water content conditions. (*D*) Molecular simulation snapshot depicting the equilibrium state of CO_2 adsorption in the pore with 50% water content. (*E*) Calcium dissolution pathways and associated free energies across different water content conditions. The free energy landscapes and configurations of key intermediate (S) and transition states (TS) during the dissolution process are illustrated. The white, red sticks, and green spheres designate hydrogen, oxygen, and calcium atoms, respectively. The dashed lines show the chemical bonds between calcium and the coordination oxygen. The energy difference between the lowest S and highest TS determines the overall energy barriers for calcium dissolution (ΔA).

interface, where water molecules are more active than in the bulk water. In addition, the diffusion coefficient of 100% water content is slightly lower than the experimentally measured diffusion coefficient of bulk water (2.3×10^{-9} m^2/s) (49) due to the low diffusion coefficient of water molecules adhering to the pore wall. It is worth noting that the free energy barrier for calcium dissolution at 16.7% water content is exceptionally high (Fig. 4*E*), suggesting that the dissolution process is unlikely to occur, and thus the carbonation process is hindered. This explains the sluggish carbonation kinetics of minerals at shallow water content in our experiments and previous studies (23, 40). The change in calcium dissolution free energy barely varies when the water content exceeds 66.7%, indicating that the water content for calcium dissolution has entered an optimal zone. Additional water has a limited effect on calcium dissolution yet leads to a sharp decline in CO_2 adsorption (Fig. 4*A*). Hence, a rough water content range of 66.7 to 83.3% is optimal for the maximum carbonation efficiency in the 4 nm CH pore.

Conclusion and Implications

The crucial importance of water in mineral carbonation is widely recognized in experimental studies and applications, yet the underlying complex mechanisms have not been fully understood. Through systematic investigation of moisture-driven carbonation kinetics, our work provides a unified framework for understanding the multifaceted role of water across diverse carbonation conditions. The carbonation rate of minerals is directly determined by the availability of reactants (metal ions and CO_2) within the medium (i.e., water), which is in turn controlled by the water-mediated dissolution and diffusion processes.

Under conditions of limited moisture content, most mesopores within the minerals are not fully saturated, creating a unique environment with coexisting solid/liquid and liquid/gas interfaces. Molecular simulations reveal a lower limit of water content (33.3%) required to reduce the mineral dissolution free energy barrier and enhance the CO_2 adsorption within the mesopores.

Within a specific range, increasing moisture content leads to a higher carbonation rate, peaking at the capillary condensation state where mineral dissolution and CO_2 docking are simultaneously promoted. Identifying such optimal moisture content (0.1 to 0.2 g/g for RCP in this study) is crucial for maximizing CO_2 mineralization efficiency in practical applications. When the moisture content exceeds the optimum, the mineral dissolution free energy is barely changed while the CO_2 intake is remarkably reduced due to the vanishment of the liquid/gas interface within the mineral pores. This causes a sharp decrease in mineral carbonation rate, which should be avoided in real-world CO_2 mineralization applications. On the other hand, at exceedingly high moisture content, saturated mesopores significantly enhance mineral dissolution and the migration of metal ions, shifting the carbonation reaction sites from internal mesopores to the external solid surface. In this case, the carbonation rate depends on the dissolution rate of CO_2 in the solution. As such, manipulating variables such as gas pressure, solution pH, and ultrasonic dispersion to modulate the concentration of CO_2 (or carbonate ions) in the solution represents an essential strategy for regulating the efficiency of CO_2 mineralization in the aqueous carbonation scenario.

Although this study focuses on the carbonation of waste concrete, the fundamental insights regarding the influence of water on carbonation mechanisms are broadly applicable to diverse mineral systems, including geological carbon sequestration, industrial mineral processing, and the weathering of natural minerals. Furthermore, the integrated experimental and computational methodology presented here provides a powerful framework for optimizing carbonation processes across a range of materials by systematically targeting maximum CO_2 mineralization efficiency.

Materials and Methods

Experimental Procedure. Ordinary Portland cement paste blocks with a water/cement ratio of 0.45 were cured for over 6 mo at room temperature before being crushed into the powder of 150 μm. The powder sample was placed on a stand at the upper opening of a cylindrical container with a diameter of 10 cm (Fig. 2*A*). An ultrasonic atomizer nozzle was positioned ~30 cm above the stand to generate a uniform mist flow with an average droplet radius of 40 μm. A double plunger pump (LSGB-ZB20) was used to control an adjustable flow rate range of 0 to 2 g/min. The mist was released above the sample, creating a mist condition with a relative humidity close to 100%. CO_2 was injected at a rate of 500 mL/min. All experiments were conducted under ambient temperature and humidity conditions. The carbonated samples were vacuum-dried at 40 degrees Celsius for 48 h before property characterization.

Property Characterization. Prior to carbonation, the oxide content analysis of the untreated sample (passing a 200-mesh sieve) was determined by Zetium X-ray fluorescence spectroscopy from Malvern Panalytical using a boric acid–rimmed substrate tableting method. Phase composition of the carbonated samples was determined by XRD analysis using a Rigaku SmartLab 9 kW diffractometer with Cu Kα radiation ($\lambda = 1.54$ Å). Data were collected over a 2θ range of 5° to 60° with a step size of 0.02° and a rate of 2°/min. Rietveld refinement was performed using HighScore Plus software to quantify phase fractions and 10% ZnO was added as an internal standard to the samples. The R-weighted pattern value for the refined fit parameters was maintained at a level below 10%. Nitrogen adsorption–desorption isotherms were obtained at −196 degrees Celsius using Micromeritics ASAP 2020, which was performed in a liquid nitrogen environment. Samples were degassed at degrees Celsius for 12 h prior to analysis. The specific surface area was calculated by the BET method from the adsorption branch of the isotherm in the relative pressure (P/P_0) range of 0 to 1.0. Pore size distribution analysis of the sample was assessed by the Barrett–Joyner–Halenda method. The spatial distribution of elements of samples (resin-embedded, polished, and coated with a thin layer of gold) was performed using a Tescan VEGA3 instrument with an X-Max N80 detector at 20 kV and a working distance of 10 mm.

Force Field and Model Construction. The Clay Force Field (ClayFF), originally developed by Cygan et al. (50), was specifically tailored for modeling hydroxide, oxyhydroxide, and clay phases. Its modified versions have been successfully extended in modeling a variety of minerals such as cementitious materials (47, 51, 52), geopolymers (53), natural rocks (54), etc. In our molecular simulations, we employed an enhanced version of ClayFF (55) that incorporates refined parameters for CO_2, enabling accurate reproduction of its adsorption characteristics.

CH was chosen here as a common representative of alkaline minerals with high carbonation reactivity. Compared to other Ca-containing alkaline minerals such as calcium silicate, C-S-H, calcium aluminate, etc., which have complex compositions and surface configurations that lead to complicated dissolution and carbonation processes, CH has a relatively simple composition and structure, making it an ideal candidate for understanding mineral carbonation at the molecular scale. The CH primitive cell with a hexagonal symmetry was converted into an orthorhombic supercell with dimensions of ~30 Å × 30 Å × 20 Å. The supercell was subjected to relaxation under the isobaric-isothermal (NPT) ensemble at 298 K and 1 bar for 1 ns before it was used to build the slit pore model with a pore width of 4 nm. Water molecules were strategically placed on both sides of the pore walls to achieve different water contents. The detailed workflow for model construction and the slit pore models with different water contents are depicted in *SI Appendix*, Figs. S5 and S6, respectively.

Simulation Procedures. The property calculations for this study were conducted using the LAMMPS (56) package, operating under the canonical (NVT) ensemble at a constant temperature of 298 K. A time step of 1 fs was chosen to ensure precision with the Nose–Hoover thermostat and barostat applied alongside the velocity-Verlet algorithm for temporal integration.

The GCMC method was utilized to facilitate CO_2 adsorption into the CH slit pores. A CO_2 pressure of 10 bar, corresponding to a chemical potential of −8.307 kcal/mol, was maintained to secure an adequate adsorption amount for statistical analysis. The adsorption simulations spanned 10 ns to achieve equilibrium, with 100 trials for molecule insertion, removal, or displacement conducted at each picosecond interval. The equilibrium CO_2 adsorption amount was determined by averaging the data from the steady period between 6 ns and 10 ns, as shown in *SI Appendix*, Fig. S7.

The well-tempered metadynamics (57) technique was employed to explore the free energy landscape of calcium dissolution from the CH surface into the water film. Although calcium ions tend to dissolve more readily from defective sites (e.g., edge or kink), the flat surface model was chosen for its simplicity and straightforward control over water film thickness. The metadynamics sampling utilized the vertical displacement of the calcium ion and its water coordination number as collective variables. A Gaussian penalty potential with a width of 0.1 and an initial height of 1.5 kJ/mol was applied, with modifications at every 150 time steps and a bias factor of 15 to ensure a smooth approach to equilibrium. The metadynamics simulations were executed with the PLUMED (58) plugin interfaced with LAMMPS.

The self-diffusion coefficient of water within the pores was calculated by analyzing the trajectories of the water molecules following a 10 ns relaxation of the surface models. The time-dependent mean squared displacement ($MSD(t)$) was calculated and fitted to the Einstein relation to derive the diffusion coefficient (D_{H_2O}):

$$D_{H_2O} = \frac{1}{2N} \lim_{t \to \infty} \frac{MSD(t)}{t}, \quad [8]$$

where N is the dimensionality that is two for the surface adsorbed water.

Data, Materials, and Software Availability. All study data are included in the article and/or *SI Appendix*.

ACKNOWLEDGMENTS. We wish to thank National Key Research and Development Program of China (Grant No. 2024YFF0508300) and the Hong Kong Polytechnic University for funding support.

Author affiliations: [a]Department of Civil and Environmental Engineering, The Hong Kong Polytechnic University, Hong Kong 999077, China; [b]Research Centre Resources Engineering Towards Carbon Neutrality, The Hong Kong Polytechnic University, Hong Kong 999077, China; and [c]Institut Européen des Membranes, CNRS and Université of Montpellier, Montpellier 34070, France

1. S. Ó. Snæbjörnsdóttir *et al.*, Carbon dioxide storage through mineral carbonation. *Nat. Rev. Earth Environ.* **1**, 90–102 (2020).
2. I. Ioannou, Á. Galán-Martín, J. Pérez-Ramírez, G. Guillén-Gosálbez, Trade-offs between sustainable development goals in carbon capture and utilisation. *Energy Environ. Sci.* **6**, 113–124 (2023).
3. J. M. Matter, P. B. Kelemen, Permanent storage of carbon dioxide in geological reservoirs by mineral carbonation. *Nat. Geosci.* **2**, 837–841 (2009).
4. X. Zhu *et al.*, Recent advances in direct air capture by adsorption. *Chem. Soc. Rev.* **51**, 6574–6651 (2022).
5. F. Winnefeld, A. Leemann, A. German, B. Lothenbach, CO2 storage in cement and concrete by mineral carbonation. *Curr. Opin. Green Sustain. Chem.* **38**, 100672 (2022).
6. M. Stillings, Z. K. Shipton, R. J. Lunn, Mechanochemical processing of silicate rocks to trap CO2. *Nat. Sustain.* **6**, 780–788 (2023).
7. X. Qian, X. Zhou, C. Hu, F. Wang, S. Hu, Role of partial limestone calcination in carbonated lime-based binders. *Cement Concrete Res.* **183**, 107572 (2024).
8. J. Yang *et al.*, Rapid wet grinding carbonation of sintering red mud for highly efficient CO2 sequestration and Cr solidification. *Chem. Eng. J.* **488**, 151134 (2024).
9. X. He *et al.*, Wet grinding carbonation technique: Achieving rapid carbon mineralization of concrete slurry waste under low CO2 flow rate. *Chem. Eng. J.* **493**, 152836 (2024).
10. M. Ren, P. Shen, Y. Tao, C.-S. Poon, Development of highly carbonation-effective calcium silicates (β-C2S): Phase evolution, microstructure, and carbonation mechanisms. *Cement Concrete Res.* **181**, 107542 (2024).
11. S.-Y. Pan *et al.*, CO2 mineralization and utilization by alkaline solid wastes for potential carbon reduction. *Nat. Sustain.* **3**, 399–405 (2020).
12. W. Heidug, F. Neele, L. Rycroft, L. Taschini, C. Ward, Geologic CO2 storage in Eastern Europe, Caucasus and Central Asia–An initial analysis of potential and policy (United Nations Economic Commission for Europe, 2021).
13. P. J. Gunning, C. D. Hills, P. J. Carey, Accelerated carbonation treatment of industrial wastes. *Waste Manage.* **30**, 1081–1090 (2010).
14. F. Xi *et al.*, Substantial global carbon uptake by cement carbonation. *Nat. Geosci.* **9**, 880–883 (2016).
15. D. N. Huntzinger, J. S. Gierke, S. K. Kawatra, T. C. Eisele, L. L. Sutter, Carbon dioxide sequestration in cement kiln dust through mineral carbonation. *Environ. Sci. Technol.* **43**, 1986–1992 (2009).
16. M. Zajac, J. Skibsted, F. Bullerjahn, J. Skocek, Semi-dry carbonation of recycled concrete paste. *J. CO2 Util.* **63**, 102111 (2022).
17. Y. Wu, H. Mehdizadeh, K. H. Mo, T.-C. Ling, High-temperature CO2 for accelerating the carbonation of recycled concrete fines. *J. Build. Eng.* **52**, 104526 (2022).
18. Y. Gao, Y. Jiang, Y. Tao, P. Shen, C. S. Poon, Accelerated carbonation of recycled concrete aggregate in semi-wet environments: A promising technique for CO2 utilization. *Cement Concrete Res.* **180**, 107486 (2024).
19. P. Shen *et al.*, Production of aragonite whiskers by carbonation of fine recycled concrete wastes: An alternative pathway for efficient CO2 sequestration. *Renew. Sustain. Energy Rev.* **173**, 113079 (2023).
20. X. Fang, D. Xuan, B. Zhan, W. Li, C. S. Poon, Characterization and optimization of a two-step carbonation process for valorization of recycled cement paste fine powder. *Construct. Build. Mater.* **278**, 122343 (2021).
21. X. Fang, D. Xuan, B. Zhan, W. Li, C. S. Poon, A novel upcycling technique of recycled cement paste powder by a two-step carbonation process. *J. Clean. Prod.* **290**, 125192 (2021).
22. M. J. Abdolhosseini Qomi, S. Zare, H. Schaef, J. Kaszuba, K. Rosso, Molecular-scale mechanisms of CO2 mineralization in nanoscale interfacial water films. *Nat. Rev. Chem.* **6**, 598–613 (2022).
23. Z. Ma *et al.*, Utilizing waste cement for carbon dioxide sequestration and capture: The role of water content on the growth of calcium carbonate. *ACS Sustain. Chem. Eng.* **12**, 2273–2288 (2024).
24. A. Morandeau, M. Thiéry, P. Dangla, Investigation of the carbonation mechanism of CH and C-S-H in terms of kinetics, microstructure changes and moisture properties. *Cement Concrete Res.* **56**, 153–170 (2014).
25. M. Zajac, I. Maruyama, A. Iizuka, J. Skibsted, Enforced carbonation of cementitious materials. *Cement Concrete Res.* **174**, 107285 (2023).
26. S. Steiner, B. Lothenbach, T. Proske, A. Borgschulte, F. Winnefeld, Effect of relative humidity on the carbonation rate of portlandite, calcium silicate hydrates and ettringite. *Cement Concrete Res.* **135**, 106116 (2020).
27. P. Shen *et al.*, Preparation aragonite whisker-rich materials by wet carbonation of cement: Towards yielding micro-fiber reinforced cement and sequestrating CO2. *Cement Concrete Res.* **159**, 106891 (2022).
28. M. Zajac *et al.*, Phase assemblage and microstructure of cement paste subjected to enforced, wet carbonation. *Cement Concrete Res.* **130**, 105990 (2020).
29. X. Fang, D. Xuan, P. Shen, C. S. Poon, Fast enhancement of recycled fine aggregates properties by wet carbonation. *J. Clean. Prod.* **313**, 127867 (2021).
30. Y. Jiang *et al.*, Mechanism of carbonating recycled concrete fines in aqueous environment: The particle size effect. *Cement Concrete Compos.* **133**, 104655 (2022).
31. C. Michel, Capillary permeability and how it may change. *J. Physiol.* **404**, 1 (1988).
32. J. Cai, Y. Chen, Y. Liu, S. Li, C. Sun, Capillary imbibition and flow of wetting liquid in irregular capillaries: A 100-year review. *Adv. Colloid Interface Sci.* **304**, 102654 (2022).
33. P. Kolliopoulos, K. S. Jochem, R. K. Lade Jr., L. F. Francis, S. Kumar, Capillary flow with evaporation in open rectangular microchannels. *Langmuir* **35**, 8131–8143 (2019).
34. J. Cai *et al.*, Lucas-Washburn equation-based modeling of capillary-driven flow in porous systems. *Langmuir* **37**, 1623–1636 (2021).
35. E. W. Washburn, The dynamics of capillary flow. *Phys. Rev.* **17**, 273 (1921).
36. Q. Tang, Z. Ma, H. Wu, W. Wang, The utilization of eco-friendly recycled powder from concrete and brick waste in new concrete: A critical review. *Cement Concrete Compos.* **114**, 103807 (2020).
37. D. Oh, T. Noguchi, R. Kitagaki, H. Choi, Proposal of demolished concrete recycling system based on performance evaluation of inorganic building materials manufactured from waste concrete powder. *Renew. Sustain. Energy Rev.* **135**, 110147 (2021).
38. E. R. Bobicki, Q. Liu, Z. Xu, H. Zeng, Carbon capture and storage using alkaline industrial wastes. *Prog. Energy Combust. Sci.* **38**, 302–320 (2012).
39. Y. Pu *et al.*, Accelerated carbonation treatment of recycled concrete aggregates using flue gas: A comparative study towards performance improvement. *J. CO2 Util.* **43**, 101362 (2021).
40. I. Galan, C. Andrade, M. Castellote, Natural and accelerated CO2 binding kinetics in cement paste at different relative humidities. *Cement Concrete Res.* **49**, 21–28 (2013).
41. D. G. Lev, K. E. Gubbins, R. Radhakrishnan, M. Sliwinska-Bartkowiak, Phase separation in confined systems. *Rep. Progress Phys.* **62**, 1573 (1999).
42. S. Zare, K. M. S. Uddin, A. Funk, Q. R. S. Miller, M. J. Abdolhosseini Qomi, Nanoconfinement matters in humidified CO2 interaction with metal silicates. *Environ. Sci. Nano* **9**, 3766–3779 (2022), 10.1039/d2en00148a.
43. S. Zare, A. Funk, M. J. Abdolhosseini Qomi, Formation and dissolution of surface metal carbonate complexes: Implications for interfacial carbon mineralization in metal silicates. *J. Phys. Chem. C* **126**, 11574–11584 (2022).
44. A. Aili, I. Maruyama, Review of several experimental methods for characterization of micro-and nano-scale pores in cement-based material. *Int. J. Concrete Struct. Mater.* **14**, 55 (2020).
45. S. Masoumi, H. Valipour, M. J. Abdolhosseini Qomi, Intermolecular forces between nanolayers of crystalline calcium-silicate-hydrates in aqueous medium. *J. Phys. Chem. C* **121**, 5565–5572 (2017).
46. P. A. Bonnaud, B. Coasne, R. J. Pellenq, Molecular simulation of water confined in nanoporous silica. *J. Phys. Condens. Matter.* **22**, 284110 (2010).
47. Y. Tao, Y. Gao, Y. Sun, R. J. M. Pellenq, C. S. Poon, C-S-H decalcification in seawater: The view from the nanoscale. *Cement Concrete Res.* **175**, 107385 (2024).
48. Y. Tao, S. Zare, F. Wang, M. J. A. Qomi, Atomistic thermodynamics and kinetics of dicalcium silicate dissolution. *Cement Concrete Res.* **157**, 106833 (2022).
49. M. Holz, S. R. Heil, A. Sacco, Temperature-dependent self-diffusion coefficients of water and six selected molecular liquids for calibration in accurate 1H NMR PFG measurements. *Phys. Chem. Chem. Phys.* **2**, 4740–4742 (2000).
50. R. T. Cygan, J.-J. Liang, A. G. Kalinichev, Molecular models of hydroxide, oxyhydroxide, and clay phases and the development of a general force field. *J. Phys. Chem. B* **108**, 1255–1266 (2004).
51. Y. Cai, Y. Tao, D. Xuan, X. Zhu, C. S. Poon, Effects of seawater on the formation and mechanical properties of Friedel's salt associated with tricalcium aluminate. *Cement Concrete Res.* **174**, 107340 (2023).
52. Y. Cai, Y. Tao, D. Xuan, Y. Sun, C. S. Poon, Effect of seawater on the morphology, structure, and properties of synthetic ettringite. *Cement Concrete Res.* **163**, 107034 (2023).
53. R. K. Mishra *et al.*, *cemff*: A force field database for cementitious materials including validations, applications and opportunities. *Cement Concrete Res.* **102**, 68–89 (2017).
54. S. Kerisit, J. H. Weare, A. R. Felmy, Structure and dynamics of forsterite–scCO_2/H_2O interfaces as a function of water content. *Geochim. Cosmochim. Acta* **84**, 137–151 (2012).
55. R. T. Cygan, V. N. Romanov, E. M. Myshakin, Molecular simulation of carbon dioxide capture by montmorillonite using an accurate and flexible force field. *J. Phys. Chem. C* **116**, 13079–13091 (2012).
56. S. Plimpton, Fast parallel algorithms for short-range molecular dynamics. *J. Comput. Phys.* **117**, 1–19 (1995).
57. A. Barducci, G. Bussi, M. Parrinello, Well-tempered metadynamics: A smoothly converging and tunable free-energy method. *Phys. Rev. Lett.* **100**, 020603 (2008).
58. M. Bonomi *et al.*, PLUMED: A portable plugin for free-energy calculations with molecular dynamics. *Comput. Phys. Commun.* **180**, 1961–1972 (2009).